

Na_{3.5}(MnVFeTi)_{0.5}(PO₄)₃: A Multi-Transition-Metal-Ion-Engineered NASICON-Type Cathodes for Sodium Ion Batteries

Vaiyapuri Soundharajan,^[a] Ghalib Alfaza,^[b] Anindityo Arifiadi,^[c] Demelash Feleke,^[c] Subramanian Nithiananth,^[d] JunJi Piao,^[b] Zhiyuan Zeng,^[e] Duong Tung Pham,^[f] Chunjoong Kim,^[a] and Jaekook Kim*^[b, g]

Electrochemically active Na-superionic conductor (NASICON)-type cathodes have the structural flexibility to include various transition elements, thus enabling high power outputs benefited by multi-electron redox reactions. This study amalgamated multiple transition metal ions to construct a new NASICON-type cathode i.e., carbon coated Na_{3.5}(MnVFeTi)_{0.5}(PO₄)₃ (NMVFTP/C) for Na-ion batteries (NIBs). The NMVFTP/C cathode engineered in this study demonstrated stable Na⁺-storage capacity, includ-

ing long-term cycling stability up to 4000 cycles at 3000 mA g⁻¹ with 96% capacity retention and a high-rate output capacity of 85.16 mA h g⁻¹ at 2500 mA g⁻¹. To elucidate the ion transport process within the cathode, density functional theory modeling was employed. The low energy barrier for the diffusion of Na⁺ in the NMVFTP/C materials was proved to be a key factor supporting our material's superior electrochemical performances.

1. Introduction

Li-ion batteries (LIBs) are often considered a critical energy source for the twenty-first century owing to their widespread use in electric vehicles, uninterruptible power supplies, smartphones, and laptops.^[1–5] However, concerns remain regarding the ability of LIBs to substitute fossil fuels and satisfy the growing societal power demands.^[6–9] This can be attributed to the limited accessibility, uneven geographic distribution, and high cost of Li.^[10–13] To address these challenges, rechargeable batteries that are economically viable, secure, and offer

consistent cycling efficiency while utilizing certain abundantly available resources must be urgently investigated.^[14,15] Replacing Li with cost-effective, widely available, and evenly distributed Na may be promising for future developments.^[16–18] Na-ion batteries (NIBs) have lower volumetric and gravimetric energy densities than LIBs; however, the former is more cost-effective for stationary and large-scale applications.^[19,20]

Thus far, energy engineers have prepared diverse cathode materials, such as Prussian blue analogues, polyanionic compounds, organic compounds, and sodiated transition metal oxides, for use in NIBs.^[21] Specifically, the Na-superionic conductor (NASICON)-type cathodes have attracted attention owing to their stable crystallographic structures, facilitating reliable storage properties in NIBs.^[11,22] Within the NASICON family, Na₃V₂(PO₄)₃ (NVP) is the most extensively studied cathode material owing to the exceptional structural and thermal stability and ionic conductivity of this material.^[23] NVP cathodes with a rhombohedral structure offer a theoretical capacity of 117.6 mA h g⁻¹ and a working potential in the range of 3.3–3.4 V.^[24–28] Nevertheless, concerns regarding V depletion, high costs, and toxicity have made researchers cautious regarding the use of NVP for energy storage.^[29] Moreover, pure NVP has poor cycling stability and rate performance owing to low electronic conductivity, which has led to the exploration of various methods for modifying NVP.^[30–32]

Transition metals, such as Fe, Ti, and Mn, are being considered as alternatives to V owing to their environmentally friendly, non-toxic, and abundant nature. The reversible redox reaction of Ti³⁺/Ti⁴⁺, Fe²⁺/Fe³⁺, and Mn²⁺/Mn³⁺ couples is significant factor in formulating new NASICON-type cathodes for NIBs.^[33–35] Goodenough et al.^[29,36] proposed a method for decreasing reliance on V using a cation-swapping technique. This method employed environmentally friendly and abundant transition metal ions, namely, Mn and Fe, in Na₄MnV(PO₄)₃

[a] V. Soundharajan, C. Kim

Department of Materials Science and Engineering, Chungnam National University, Daejeon 34134, Republic of Korea

[b] G. Alfaza, J. Piao, J. Kim

Department of Materials Science and Engineering, Chonnam National University, 77 Yongbong-ro, Bukgu, Gwangju 61186, Republic of Korea
E-mail: jaekook@chonnam.ac.kr

[c] A. Arifiadi, D. Feleke

MEET Battery Research Center, Institute of Physical Chemistry, Westfälische Wilhelms-Universität Münster, Münster, Corrensstraße 46, 48149 Germany

[d] S. Nithiananth

Graduate School of Science and Technology, Shizuoka University, 3-5-1 Johoku, Naka-ku, Hamamatsu, Shizuoka, 432-8011, Japan

[e] Z. Zeng

Department of Materials Science and Engineering, City University of Hong Kong, 83 Tat Chee Avenue, Kowloon, Hong Kong 999077, China

[f] D. T. Pham

School of Engineering Physics, Hanoi University of Science and Technology, No 1 Dai Co Viet Street, 100000, Hanoi, Viet Nam.

[g] J. Kim

Research Center for Artificial Intelligence Assisted Ionics Based Materials Development Platform, Chonnam National University, Gwangju, 61186, Republic of Korea

 Supporting information for this article is available on the WWW under <https://doi.org/10.1002/batt.202400526>

(NMVP) and $\text{Na}_3\text{VFe}(\text{PO}_4)_3$. The study revealed that including Mn reduced costs and increased the operational voltage. Additionally, the inclusion of V reduced the Jahn–Teller distortion in Mn^{3+} during charging, thereby guaranteeing the structural stability of the material during repeated cycling.^[36] Whilst NMVPs have good electrochemical properties within a controlled upper breakdown voltage (≈ 4.0 V), their electrochemical properties are poor beyond 4.0 V due to irreversible structural changes. Whereas the extraction of Na^+ ions from the NMVP structure above 4.0 V offers a means of enhancing charge capacity, the process of reversible insertion of Na^+ ions back into the structure is significantly impeded by the structural transformations that occur during the charging phase when the voltage surpasses the 4.0 V threshold.^[11] Indeed, the upper cut-off range above 4.0 V has not been suitable for practical applications of NMVP cathodes and has been referred to as the irreversible voltage range.^[11] The use of high and intermediate entropies, a common tactic in layered oxide cathodes, has been extended to NASICON-type NMVP cathodes where transition metals are combined to stabilize the structure.^[37–40] The incorporation of supplementary metal components into the NMVP-derived cathode materials enables the attainment of reliable Na^+ storage properties exceeding the 4.0 V threshold limits.^[27,34]

To our surprise, the Li group has only recently reported a $\text{Na}_{3.5}(\text{MnVFeTi})_{0.5}(\text{PO}_4)_3$ cathode, which means that our cathode also has a structural similarity.^[34] However, as the synthesis methodology and theoretical studies carried out in this work will optimize the approach for the practical characteristics of the proposed cathode, we believe it is essential to discuss the outcome of this work in this report. The polyol-assisted pyrolysis technique is known to produce functional nanoparticles in a very short reaction time under open-air conditions. The polyol solvent serves as a source of conductive carbon coating, which is essential for facilitating Na^+ ion movement in NASICON-type cathodes.

Thus, this study has successfully formulated a multi-element engineered $\text{Na}_{3.5}(\text{MnVFeTi})_{0.5}(\text{PO}_4)_3$ cathode with a stable *in situ* carbon coating (NMVFTP/C) via the rapid pyro-synthesis technique. The NMVFTP/C exhibits a stable Na^+ storage behaviour between 4.2 and 1.5 V. On the other hand, the pristine NMVP/C compared in this study could not reversibly (de)incorporate the Na^+ ions into the structure and the cycle lifetime ended after a few cycles. The combined experimental and theoretical study revealed that Na^+ storage mechanism is controlled by single/biphasic transitions. The multi-electron transition elements in the NMVFTP/C structure (V^{3+} , Mn^{2+} , Fe^{2+} , and Ti^{4+}) provided a high discharge capacity of 141.42 mAh g⁻¹ and a stable working voltage output of 3.4 V, thus inducing a material-level specific energy output of 480.82 Wh kg⁻¹. We believe that the remarkable energy and electrochemical performance of NMVFTP/C could innovate the design of rational NASICON-type cathodes for next-generation NIBs.

2. Result and Discussion

Engineering a V-less NASICON-type cathode has been the main research focus around NASICON cathodes for NIBs. To confirm the successful engineering of Mn, Fe, and Ti into the NASICON phosphate crystal to form NMVFTP/C, we conduct high-resolution X-ray diffraction (HRXRD) measurements on the carbon-coated powder, as shown in Figure 1a. The results obtained from the Rietveld refinement process have confirmed that the NMVFTP/C sample that originated from the multi-substituent elements can be identified as a NASICON-type structure.^[41]

The Rietveld refinement further confirmed that NMVFTP/C has a rhombohedral structure ($a=b=8.8241$, $c=21.6731$, $V=1461.478578 \text{ \AA}^3$) with an R-3c space group (Table S1). Moreover, $R_{wp}=2.80\%$, $R_{exp}=2.19\%$, $\chi^2=1.6347$, and $\text{GOF}=1.2785$ further confirmed the purity of the refinement parameters. The crystal structure of the prepared multi-transition-metal-ion-engineered NMVFTP/C cathode is illustrated in Figure 1b,c. Here, the crystal comprises corner-shared TMO_6 ($\text{TM}=\text{Mn, V, Fe, and Ti}$) octahedral and PO_4 tetrahedral units, with Na^+ occupying two different sites between (Na (1) and Na (2)) along the c-axis, facilitating the process of Na diffusion.^[42]

The high-resolution transmission electron microscopy (HRTEM) of NMVFTP/C powder was observed to have a micro-disc-like morphology (Figure 2a). In addition, we have carried out HRTEM analysis on NMVFTP/C as shown in Figure 2b. The results indicate that the NMVFTP/C crystal has interplanar spacings of 0.25 and 0.62 nm, which can be associated with the (300) and (012) planes of the rhombohedral crystal, respectively. Further, crystallographic analysis was performed via selected area electron diffraction (SAED) using the Crystbox tool.^[43] The results are presented in Figure 2c, which confirms the diffraction spots originating from the (410), (116), (006), (113), (012), and (300) planes, supporting the HRXRD result presented earlier.

Figure 2d shows the energy dispersive spectroscopy (EDS) mapping that was carried out to investigate the distribution of the elements within the NMVFTP/C sample. Na, Mn, V, Fe, Ti, P, O and C are uniformly distributed throughout the NMVFTP/C sample as confirmed by the mapping results. A close investigation of the carbon structure using Raman spectroscopy, as shown in Figure 3a, reveals the presence of two characteristic peaks at 1351 cm^{-1} (D-band) and 1592 cm^{-1} (G-band). An intensity ratio (I_D/I_G) of ≈ 0.86 indicates that the carbon coating was partially graphitized.^[44] Using thermogravimetric analysis, as shown in Figure 3b, the carbon content in NMVFTP/C was estimated to be 7.9 wt%, which should be sufficient to provide adequate electronic conductivity to the NASICON structure.

Figure 3c–f displays the spectra obtained via high-resolution X-ray photoelectron spectroscopy (HRXPS) of NMVFTP/C, providing insights into both its chemical composition and valence states. Figure 3c demonstrates the presence of two distinct peaks in the Mn 2p spectrum. The binding energy peaks corresponding to $\text{Mn } 2p_{1/2}$ and $\text{Mn } 2p_{3/2}$ were observed at 652.7 and 640.8 eV, respectively. The conspicuous $\text{Mn } 2p_{3/2}$ peaks can be resolved into two distinct peaks at 644.0 and 640.8 eV.

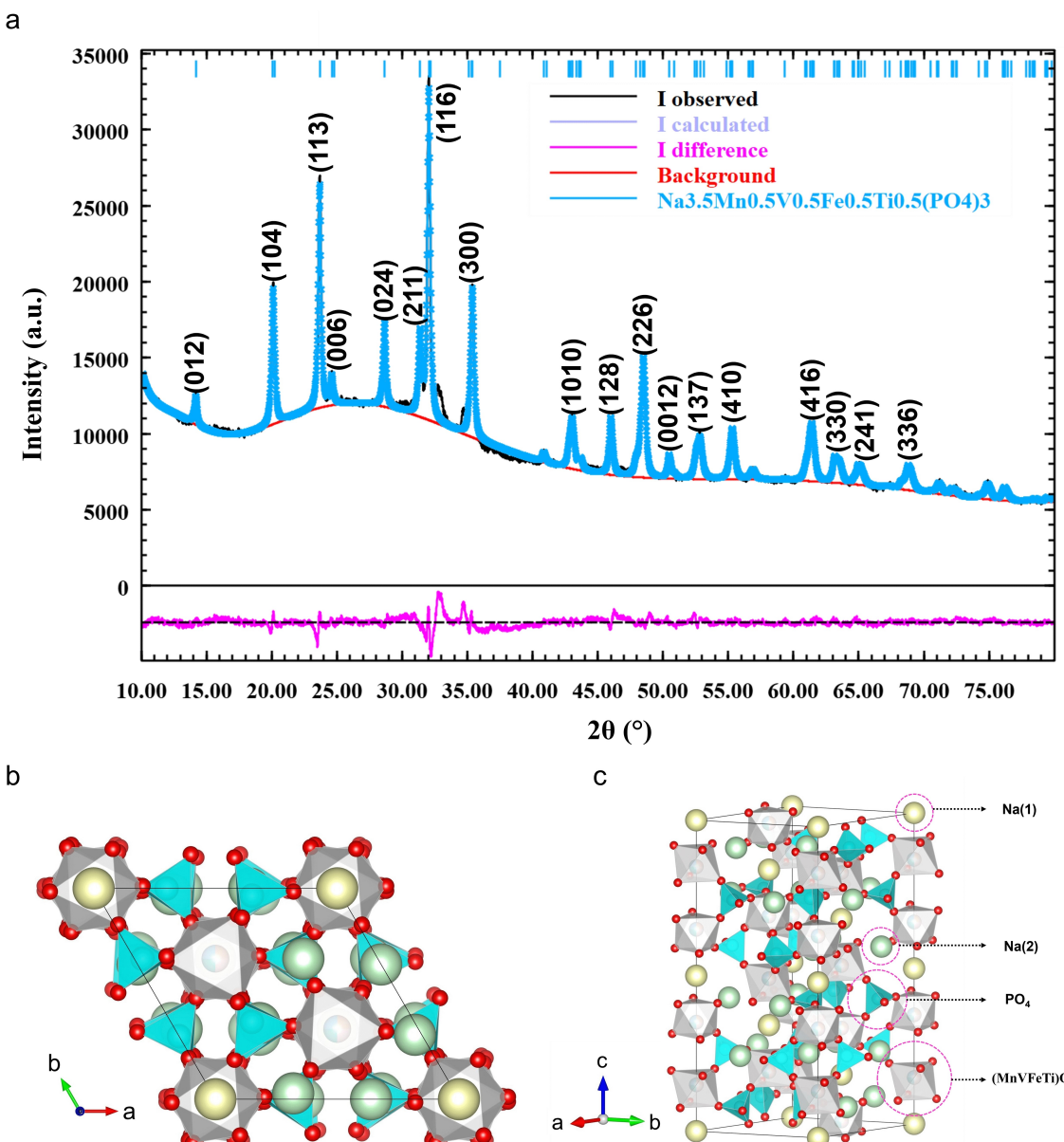


Figure 1. Physicochemical results obtained from the active material of a) Rietveld pattern of NMVFTP/C, (b) The Rietveld refinement of NMVFTP/C crystal structure along the c-axis of Na and c) Crystal structure of NMVFTP/C.

Likewise, Mn $2p_{1/2}$ peaks can be resolved into two distinct peaks at 657.7 and 652.7 eV, which can be attributed to Mn $^{3+}$ and Mn $^{2+}$, respectively.^[45] The XPS spectra of V 2p depicted in Figure 3d indicates the presence of mixed valence states of V. The observed peaks at 522.98, 521.68 eV for V 2p $_{1/2}$ and 516.18, 517.4 eV for V 2p $_{3/2}$ can be attributed to either trivalent or tetravalent V species, i.e., V $^{4+}$ and V $^{3+}$.^[29] Figure 3e displays the XPS spectra of Fe 2p containing two symmetrical peaks. Figure 3e shows the XPS peaks at 710.9, 714.9 and 724.2, 729.3 eV binding energies, corresponding to Fe $^{2+}$ and Fe $^{3+}$ for Fe 2p $_{3/2}$ and Fe 2p $_{1/2}$, respectively. These findings provide evidence for the presence of Fe $^{3+}$ in the sample.^[46] Two prominent peaks were observed at approximately 464.7 and 458.8 eV, corresponding to the Ti 2p $_{1/2}$ and Ti 2p $_{3/2}$ orbitals,

respectively (Figure 3f).^[47] The observed peak splitting value of the Ti 2p is determined to be 5.3 eV, suggesting the presence of Ti in a Ti $^{4+}$ valence state.^[29] The high-resolution XPS spectra of Na display a distinctive peak at 1071.1 eV, corresponding to Na 1s, as shown in Figure S1a.^[48] Figure S1b shows the C 1s XPS spectrum with peaks observed at 283.6, 284.6, 285.5, and 288.6 eV, corresponding to the C–C, C=C, C–O, and O–C=O, respectively.^[49,50]

In Figure S1c, the O 1s spectra reveal three distinct peaks at 530.1, 531.6, and 534.9 eV, which are associated with V–O, C–O, and C–OH, respectively.^[51,52] The two major peaks of P 2p at 132.2 and 133.1 eV, which corresponds to the P 2p $_{3/2}$ and P 2p $_{1/2}$, respectively (Figure S1d).

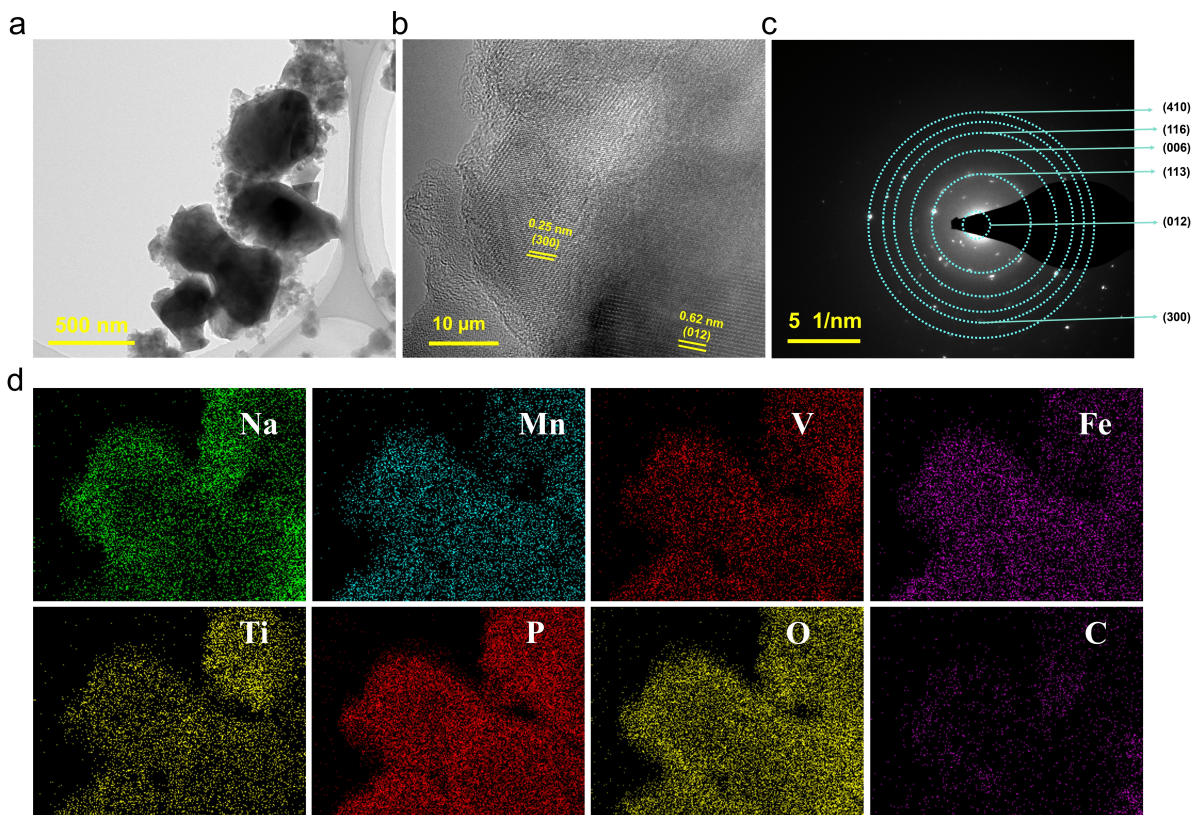


Figure 2. a) High-resolution transmission electron microscope (HRTEM) image of NMVFTP/C, b) HRTEM image of the NMVFTP/C lattice fringe, c) Selected area electron diffraction (SAED) pattern of NMVFTP/C and d) EDS mapping of NMVFTP/C.

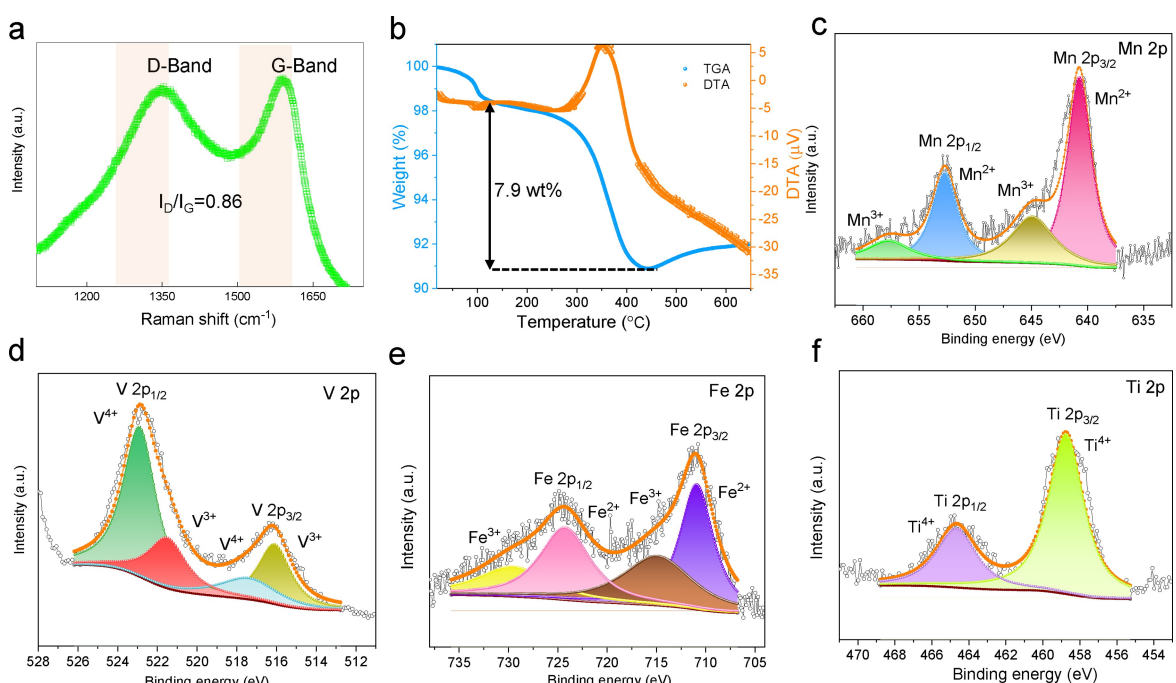


Figure 3. a) Raman profile of NMVFTP/C, b) Thermogravimetric profile of NMVFTP/C, XPS profile of the NMVFTP/C sample: c) Mn 2p, d) V 2p, e) Fe 2p, and f) Ti 2p.

As a reference material, carbon-coated $\text{Na}_4\text{MnV}(\text{PO}_4)_3$ (NMVP/C) documented earlier by our group is utilized for

comparison.^[26] Figure 4a presents the cyclic voltammetry (CV) results obtained from NMVFTP/C and NMVP/C cathodes at

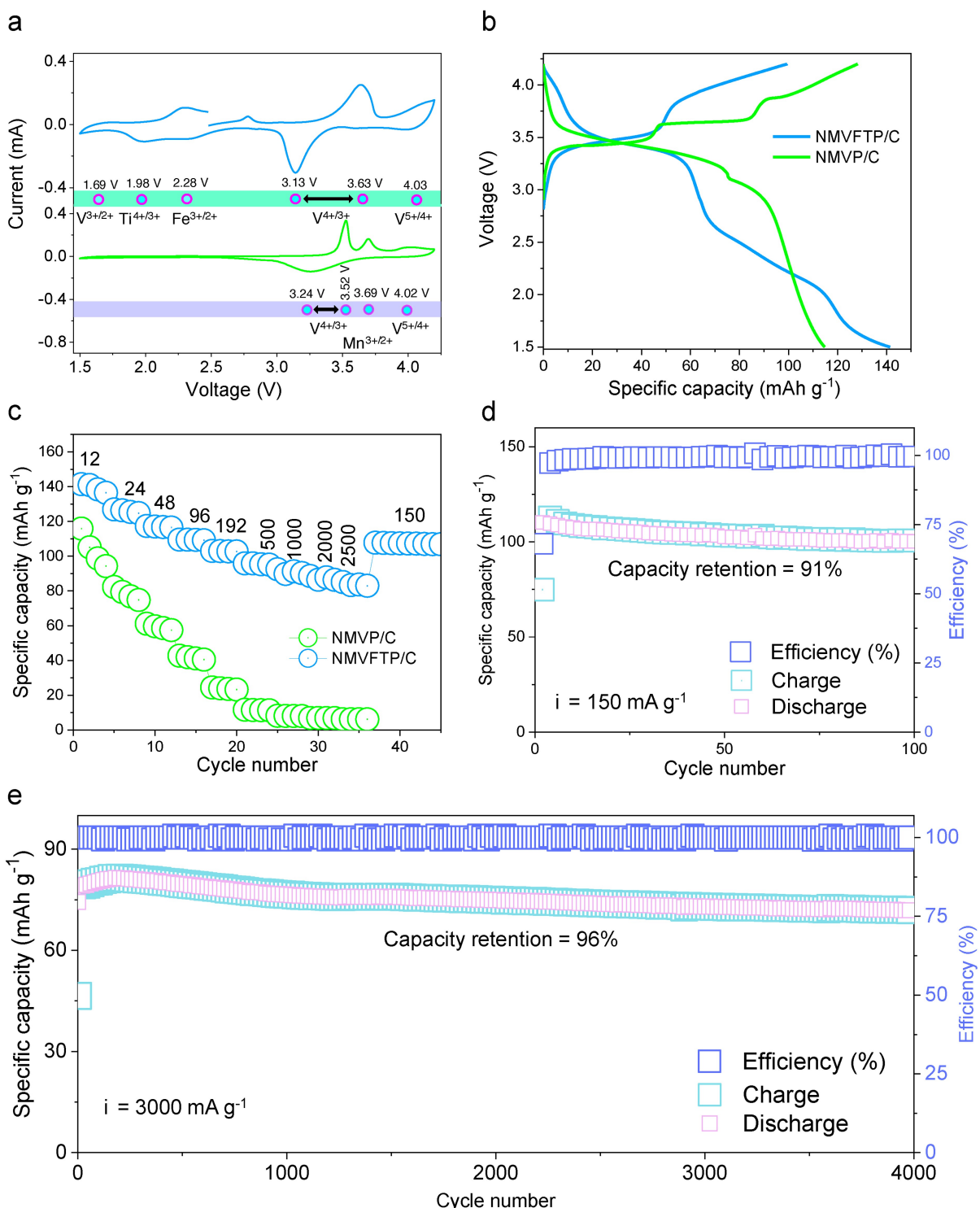


Figure 4. Electrochemical Na⁺-storage performance in the half-cell configuration, a) CV profile obtained from the NMVFTP/C and NMVP/C cathodes at 0.2 mV s⁻¹ between 4.2–1.5 V, b) Galvanostatic charge/discharge profile of the NMVFTP/C and NMVP/C cathode at 12 mA g⁻¹, c) Rate performance evaluation of the NMVFTP/C and NMVP/C cathode. Cycle life curve of the NMVFTP/C cathode at d) 150 mA g⁻¹ and e) 3000 mA g⁻¹.

0.2 mV s⁻¹ between 4.2–1.5 V in an NMVFTP/C | Na cell. During the positive sweep, the NMVFTP/C cathode yielded the first oxidation peak at ≈ 2.8 V and a broad peak at ≈ 3.5 V ($V^{3+/4+}$ and $Mn^{2+/3+}$), followed by a half peak at >3.8 V ($V^{4+/5+}$).^[27] In contrast, for the NMVP/C cathode, the broad peaks at 3.52 and

≈ 3.69 V could be associated with the $V^{3+/4+}$ and $Mn^{2+/3+}$ redox pairs, the $V^{4+/5+}$ peak at 3.8 V is less intense.^[53] During the negative sweep, while the NMVP/C cathode has only one broad reduction peak at ≈ 3.3 V, the NMVFTP/C cathode exhibits additional peaks, originating from the Ti^{4+} to Ti^{3+} and V^{3+} to

V^{2+} reductions, at low voltages between 1.5–2.4 V. The low redox potential of Ti^{4+}/Ti^{3+} (2.1 V) and V^{3+}/V^{2+} (1.7 V) with respect to the open circuit potential (OCP) of ≈ 2.45 V of the NMVFTP/C explains the absence of the Ti^{4+}/Ti^{3+} and V^{3+}/V^{2+} oxidation peaks during the first positive sweep from the OCP and the presence of these peaks during the positive sweep from 1.5 V. In addition, no specific peak for the $Mn^{2+/3+}$ redox pair was observed for the NMVFTP/C cathode. Instead, the broad peaks (3.13 and 3.63 V) observed during the positive and negative scans, with a clear displacement compared to the original NMVP/C cathode, could be related to the combination of $Mn^{2+/3+}$ and $V^{3+/4+}$ redox pairs, as observed in the previous reports.^[29]

The impact of multi-element engineering can be seen in the voltage profile of the NMVFTP/C cathode, as presented in Figure 4b. While the NMVP/C cathode delivers a discharge capacity that is 114.73 mAh g⁻¹ lower than its charge capacity (128.12 mAh g⁻¹), the discharge capacity of the NMVFTP/C cathode is 141.42 mAh g⁻¹ higher than its charge capacity (99.37 mAh g⁻¹) due to the discharge capacity contribution from $Ti^{4+}/Fe^{3+}/V^{3+}$ reduction. Furthermore, Figure 4c shows the superior rate performance of the NMVFTP/C cathode. The specific capacities of the NMVFTP/C cathode were found to be 141.42, 126.92, 117.37, 109.53, 103.05, 95.88, 92.48, 88.61, and 85.16 mAh g⁻¹ at current rates of 12, 24, 48, 96, 192, 500, 1000, 2000, and 2500 mA g⁻¹, respectively. Whereas the average specific capacities of the NMVP/C cathode were found to be 115.87, 82.30, 61.15, 42.74, 24.50, 11.69, 8.90, 6.91, and 6.87 mAh g⁻¹ at current rates of 12, 24, 48, 96, 192, 500, 1000, 2000, and 2500 mA g⁻¹, respectively, which is inferior to the NMVFTP/C outputs.

The superior performance of the NMVFTP/C cathode is further demonstrated via long-term cycling tests, as shown in Figure 4d–e. When cycled at 150 mA g⁻¹, the NMVFTP/C cathode retained 91% of its initial capacity (110.2 mAh g⁻¹) after 100 cycles, with a coulombic efficiency of 99.12%. The selected galvanostatic charge/discharge profile of the NMVFTP/C cathode is provided in the Figure S2a, indicates a stable Na⁺ storage behavior. After assessing the cycle life of the NMVFTP/C cathode at a low current rate, the rapid Na⁺-storage ability is further evaluated at a high specific current of 3000 mA g⁻¹, and the cycle life profile is provided in Figure 4e. Additionally, the instant (de)sodiation features of the NMVFTP/C cathode were promising, i.e., the NMVFTP/C cathode delivered a stable specific discharge capacity of 74.3 mAh g⁻¹ and retained a capacity of 71.8 mAh g⁻¹, thereby validating a 96% capacity retention after 4,000 cycles. Also, the constant voltage profiles for the selected galvanostatic charge/discharge profile (Figure S2b) at such a high current rate show that the NMVFTP/C cathode is durable.

To explain the superior kinetics of the NMVFTP/C cathode, CV measurements with increasing sweep rates in the range of 0.1–1.0 mV s⁻¹ are presented in Figure S3a. Four reversible redox pairs represent the contribution of different redox couples present in the NMVFTP/C cathode. At a specific voltage, two Na-storage mechanisms, i.e., diffusion and capacitive contributions, are possible. The relation between current and voltage

can be described according to Equations (1) and (2), in which the measured current (i) correlates with the applied scan rate (v) based on the power law.^[54,55]

$$i = av^b, \quad (1)$$

$$\log i = b \log v + \log a, \quad (2)$$

$$i = k_1 v + k_2 v^{0.5}, \text{ where } k_1 + k_2 = 1. \quad (3)$$

The two extreme b values are 0.5 and 1.0, representing the ideal diffusion- and capacitive-controlled storage mechanism, respectively. By plotting $\log i$ versus $\log v$, we obtained b values of 0.78, 0.68, 0.85, 0.77, 0.88, and 0.66 for voltages peaks at 3.505, 4.100, 2.301, 4.035, 3.335, and, 1.998 V respectively. The b values obtained for the charge and discharge reactions indicate that the capacitive-controlled processes are dominant in the Na-storage mechanism in the NMVFTP/C cathode (Figure S3b). Equation (3) is used to calculate the ratio of diffusion- (k_2) and capacitance-related (k_1) capacities related to each peak, and a representative result showing the separated capacity contribution is shown in Figure S3c. We further calculate the ratio of both capacity contributors at different scan rates, as presented in Figure S3d. Here, we noticed that the contribution from diffusion-related processes is limited at scan rates of 0.2, 0.3, 0.4, 0.5, 0.7, and 1.0 mV s⁻¹ was 48.56, 52.68, 56.28, 59.27, 63.01, and 67.47%, respectively. Thus, the CV analysis validates the capacity outputs originating from the capacitive-controlled reactions, implying the rapid Na-storage capability of the NMVFTP/C cathode.

A thorough understanding of the diffusion properties of the electrode materials is essential for accurately assessing the reaction kinetics and their role in enabling fast charging. It is possible to determine the Na⁺ diffusion coefficient (D_{Na}) using basic electrochemical techniques, including cyclic voltammetry and the galvanostatic intermittent titration technique (GITT). For example, CV curves at different scan rates facilitate the determination of D_{Na} , through the utilization of the Randles-Sevick equation to ascertain the relationship between the peak current intensity (i_p) and the square root of the scan rate ($v^{1/2}$) as follows.^[56]

$$i_p = 2.69 \times 10^5 n^{3/2} A C \sqrt{D} v$$

Where i_p is the peak current (A) and n , A , C , D , and v are the number of moles of electron, geometric area of the electrode (cm²), molar volume (cm³ mol⁻¹), D is the Na-diffusion coefficient (cm² s⁻¹) and, v is the scan rate during the CV measurement of the NMVFTP/C cathode, respectively. We fit the i_p values for reduction/oxidation peaks vs $v^{1/2}$ with a linear behavior, as shown in the Figure S4 and the slope are calculated. The Na-diffusion coefficient was estimated to be in the ranges of 2.85×10^{-10} and 1.96×10^{-10} cm² s⁻¹ for anodic and cathodic peaks at different scan rate for V redox couple, respectively. Moreover, the diffusion coefficients for the anodic and cathodic peaks at different scan rates are presented in Table S2. As the scan rate increases, the diffusion coefficients

decrease, indicating that the NMVFTP/C cathode exhibits rapid rate reaction kinetics at higher scan rates.

We further conducted the GITT to quantify the Na migration kinetics, the result is shown in Figure S5a. GITT was performed within a voltage window of 4.2–1.5 V with a specific current of 30 mA g^{-1} for 10 mins intervals for each pulse. The cell was rested for 2 h after every pulse application to obtain a quasi-equilibrium state. We used Fick's second law, as expressed in Equation (4), to estimate the Na-diffusion coefficient based on the transient voltage established during the GITT experiment.^[57]

$$D_{\text{Na}} = \frac{4}{\pi \tau} \left(\frac{m_b V_m}{M_w A} \right)^2 \left(\frac{\Delta E_s}{\Delta E_r} \right)^2 \quad (4)$$

Where D_{Na} is the Na-diffusion coefficient ($\text{cm}^2 \text{s}^{-1}$) and m_b , V_m , M_w , and A are the mass loading (g), molar volume ($\text{cm}^3 \text{mol}^{-1}$), molecular weight (g mol^{-1}), and surface area (cm^2) of the NMVFTP/C cathode, respectively. Furthermore, τ (s) represents the duration of the applied current pulse, and ΔE_s and ΔE_r are the voltage differences under the steady-state and current pulse conditions, respectively. The calculated D_{Na} values corresponding to each Current pulse during the charge and

discharge process are shown in Figure S5b,c. The Na-diffusion coefficient was estimated to be in the ranges of 2.82×10^{-8} – 9.99×10^{-11} and 1.13×10^{-8} – $2.3 \times 10^{-9} \text{ cm}^2 \text{s}^{-1}$ for Na deintercalation and intercalation, respectively. During discharge, we observed D_{Na} fluctuations at 2.2, 2.6, 3.2, and 4.0 V, confirming the participation of the $\text{V}^{2+}/\text{V}^{3+}$, $\text{Ti}^{3+}/\text{Ti}^{4+}$, $\text{V}^{3+}/\text{V}^{4+}$ /Mn²⁺/Mn³⁺, and $\text{V}^{4+}/\text{V}^{5+}$ redox couples, respectively, participating in the charge compensation process during Na intercalation.

A Ragone plot was constructed to compare the specific energies and power outputs of the NMVFTP/C cathode with those of the metal-ion-reconstructed NASICON-type cathode for NIBs (Figure 5a). The high specific energy outputs of 480.82 and $289.32 \text{ Wh kg}^{-1}$ at specific power rate of 41 and 7106 W kg^{-1} , respectively, are comparable to those of the NASICON-type cathode materials such as $\text{Na}_3\text{MnHf}(\text{PO}_4)_3$,^[58] $\text{Na}_4\text{MnCr}(\text{PO}_4)_3$,^[59] $\text{Na}_2\text{VTi}(\text{PO}_4)_3$,^[60] $\text{Na}_3\text{VAl}_{0.2}\text{Cr}_{0.2}\text{Fe}_{0.2}\text{In}_{0.2}\text{Ga}_{0.2}(\text{PO}_4)_3$,^[40] $\text{Na}_3(\text{Ti}_{0.2}\text{V}_{0.2}\text{Mn}_{0.2}\text{Cr}_{0.2}\text{Zr}_{0.2})_2(\text{PO}_4)_3$,^[61] $\text{Na}_3\text{ZrMn}(\text{PO}_4)_3$,^[24] and $\text{Na}_3\text{V}_{1.9}(\text{Ca},\text{Mg},\text{Al},\text{Cr},\text{Mn})_{0.1}(\text{PO}_4)_2\text{F}_3$.^[62]

Furthermore, the NMVFTP/C cathode exhibits superior electrochemical performance with respect to the other metal-ion-engineered NASICON-type cathodes for NIBs. It is not appropriate to make direct comparisons between the electro-

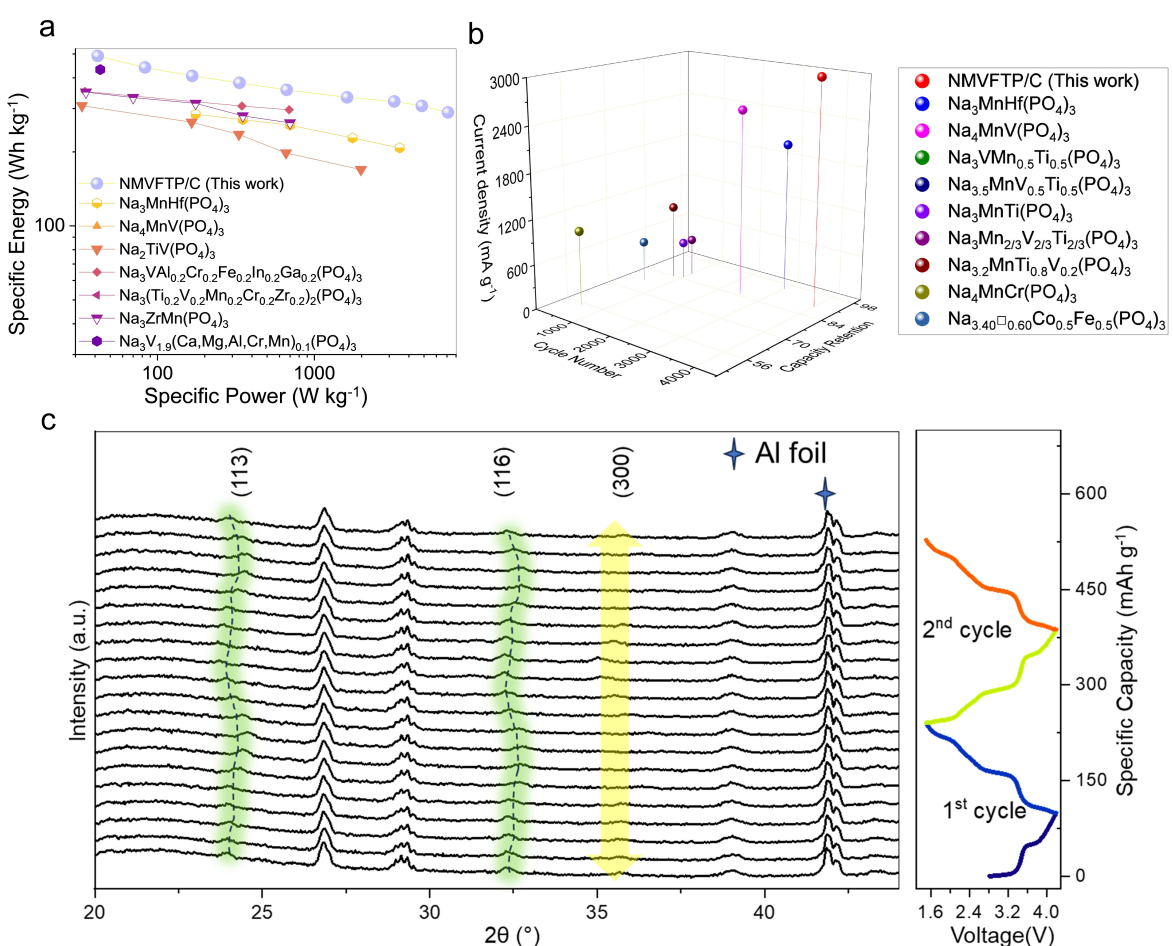


Figure 5. a) Ragone plot comparing the specific energies and power outputs of the NMVFTP/C cathode with those of the NASICON-type cathodes reported for NIBs in the literature, b) Comparison between the electrochemical performance of the NMVFTP/C cathode with those of the NASICON-type cathodes, c) Electrochemical stability and structural evolution. *Operando* X-ray diffraction outputs of NMVFTP/C at different charge/discharge depths at 30 mA g^{-1} for the initial two cycles.

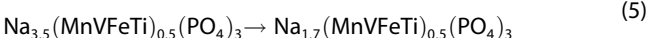
chemical performance of the NMVFTP/C cathode investigated in this study and the cathodes documented by other research teams. This is due to differences in synthesis conditions, voltage windows and electrolyte composition used by the various groups. Nevertheless, a more detailed understanding of how transition metal ions affect energy and power outputs could be gained by comparing the electrochemical properties of the NMVFTP/C cathode. For instance, the electrochemical performance, including life-cycle, current rate, and capacity retention of the NMVFTP/C cathode is further compared in Figure 5b, with the recent transition-metal-ion-engineered NASICON-type cathodes such as $\text{Na}_3\text{MnHf}(\text{PO}_4)_3$,^[58] $\text{Na}_4\text{MnV}(\text{PO}_4)_3$,^[63] $\text{Na}_3\text{VMn}_{0.5}\text{Ti}_{0.5}(\text{PO}_4)_3$,^[29] $\text{Na}_3\text{MnTi}(\text{PO}_4)_3$,^[64] $\text{Na}_{3.5}\text{Fe}_{0.5}\text{VCr}_{0.5}(\text{PO}_4)_3$,^[65] $\text{Na}_{3.2}\text{MnTi}_{0.8}\text{V}_{0.2}(\text{PO}_4)_3$,^[66] $\text{Na}_4\text{MnCr}(\text{PO}_4)_3$,^[59] $\text{Na}_{3.4\Box 0.60}\text{Co}_{0.5}\text{Fe}_{0.5}\text{V}(\text{PO}_4)_3$,^[67] and $\text{Na}_3\text{Mn}_{2/3}\text{V}_{2/3}\text{Ti}_{2/3}(\text{PO}_4)_3$ ^[39] for NIBs, where the electrochemical properties of the NMVFTP/C cathode is worthwhile.

To elucidate the structural evolution during the electrochemical cycling of the NMVFTP/C cathode, this study conducted an *Operando* X-ray diffraction (XRD) experiment, and the results are presented in Figure 5c. The special *Operando* cell was charged to 4.2 V and subsequently discharged to 1.5 V for two cycles at a specific current of 30 mA g^{-1} , as shown in the voltage profile displayed in Figure 5c. The corresponding 2D contour plots originating from different crystallographic planes are shown in Figure 5c. Overall, a gradual shift of the (113), (116), and (300) reflections to high 2θ values can be observed during charging to 4.2 V. In contrast, those reflections shifted back to low 2θ values during the discharge to 1.5 V. More specifically, the shifts in the (113) and (116) reflections were observed without any disappearance of the respective peaks, suggesting that the transformation mechanism during the Na (de)intercalation process involves the solid-solution phase. Additionally, we noticed the disappearance of the (300) reflection during charging and their subsequent appearance during discharging, implying the presence of two-phase transformation processes. In summary, the *Operando* XRD experiment revealed that the solid-solution and two-phase phase transformation processes both participate in the Na-storage mechanism in the NMVFTP/C cathode, similar to those in the NASICON-type cathodes reported previously.^[59,68,69] Using the galvanostatic charge/discharge profile and the *Operando* XRD results, we estimated that 1.8 Na^+ was intercalated after the first charging process. Subsequently, 2.5 Na^+ participated in the following charge/discharge process.

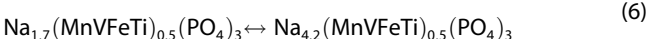
In order to gain a comprehensive insight into the alterations in the valence states of Mn, V, Fe and Ti throughout the charge and discharge cycles, ex-situ XPS was conducted on the NMVFTP/C electrode. Figure S6a-d illustrates the redox changes for Mn 2p, V 2p, Fe 2p, and Ti 2p during the second charge/discharge process. The Mn 2p peaks exhibited the following behavior during the charging and discharging processes: 641.6 eV (Mn^{2+})/644.6 eV (Mn^{3+})/653.7 eV (Mn^{2+})/657.1 eV (Mn^{3+}) for charging; and 641.4 eV (Mn^{2+})/645.3 eV (Mn^{3+})/653.4 eV (Mn^{2+})/656.8 eV (Mn^{3+}) for discharging (Figure S6a). The slight alterations in the Mn 2p peaks between the 4.2–1.5 V range imply the involvement of Mn in the Na^+ charge and

discharge processes to a limited extent.^[29] The alterations in the valence state of V 2p are demonstrated in Figure S6b and are accompanied by the corresponding binding energy peaks during the charge and discharge processes. Upon charging to 4.2 V (Figure S6b), the V 2p_{3/2} and V 2p_{1/2} peaks shift slightly toward higher binding energies at 514.9/515.9/516.8 eV and 522.5/523.5/524.7 eV, confirming the co-existence of V^{3+} , V^{4+} , and V^{5+} , respectively. Following the discharge to 1.5 V (Figure S6b), the V 2p_{3/2} peak emerges at 515.1 eV (V^{3+}), resulting from the reduction of V^{5+} to a lower oxidation state.^[35] These observations indicate that the oxidation changes are concentrated around the V 2p activity in the context of the Na^+ de-/intercalation process. The ex-situ XPS analysis of Fe 2p during the charge/discharge process of NMVFTP/C is illustrated in Figure S6c. It can be observed that the splitting and merging of peaks observed during charging (710.6 eV for Fe^{2+} , 713.4 eV for Fe^{3+} , and 717.2 eV for Fe^{4+}) and discharging (709.1 eV for Fe^{2+} , 711.9 eV for Fe^{3+} , and 718.9 eV for Fe^{4+}) highlights the role of the $\text{Fe}^{3+}/\text{Fe}^{2+}$ redox couple in regulating Na^+ transport within the NMVFTP/C cathode.^[35] The Ti 2p peaks show distinct shifts during charging and discharging. During the charging process, the peaks were observed at 458.8 eV (Ti^{3+}) and 464.4 eV (Ti^{4+}). During the discharging process, the peaks begin at 457.6 eV (Ti^{3+}) and 465.4 eV (Ti^{4+}).^[29] These findings demonstrate the involvement of the $\text{Ti}^{4+}/\text{Ti}^{3+}$ redox couple in regulating the Na^+ insertion within the NMVFTP/C cathode (Figure S6d). Based on the combined electrochemical and structural analysis using the in situ XRD and ex situ XPS analysis, the reactions during the first charge and the following charge/discharge cycles are expressed in Equations (5) and (6) (Figure S7).

Firstcharge :



Subsequentcycles :



For further investigations, we conducted first-principle calculations to elucidate the intercalation mechanism in NMVFTP materials. Figure 6a shows the calculated convex hull plot of $\text{Na}_x(\text{MnVFeTi})_{0.5}(\text{PO}_4)_3$ with the corresponding intercalation potential. Based on the plot, we identify that no abnormal behaviour occurs, which is often associated with strong compositional inhomogeneity in cathode particles, leading to large stresses and concomitant capacity degradation.^[70] Notably, even though we could not identify any ground states of $\text{Na}_2(\text{MnVFeTi})_{0.5}(\text{PO}_4)_3$, we argue that the phase was stable because this phase was situated below 26 meV/atom above the hull (thermal energy component at room temperature).^[71]

Theoretical voltage profiles are predicted from the convex hull plots, where the redox pairs $\text{Ti}^{3+}/\text{Ti}^{4+}$, $\text{Fe}^{2+}/\text{Fe}^{3+}$, $\text{V}^{3+}/\text{V}^{4+}/\text{V}^{5+}$, and $\text{Mn}^{2+}/\text{Mn}^{3+}$ are identified as the source of Na^+ electrochemical activity, consistent with the electrochemical response observed from the CV and galvanostatic observations. The density functional theory (DFT) calculations estimated the voltage curve by computing the energy associated with a restricted set of Na concentrations. Only the local average voltage can be deter-

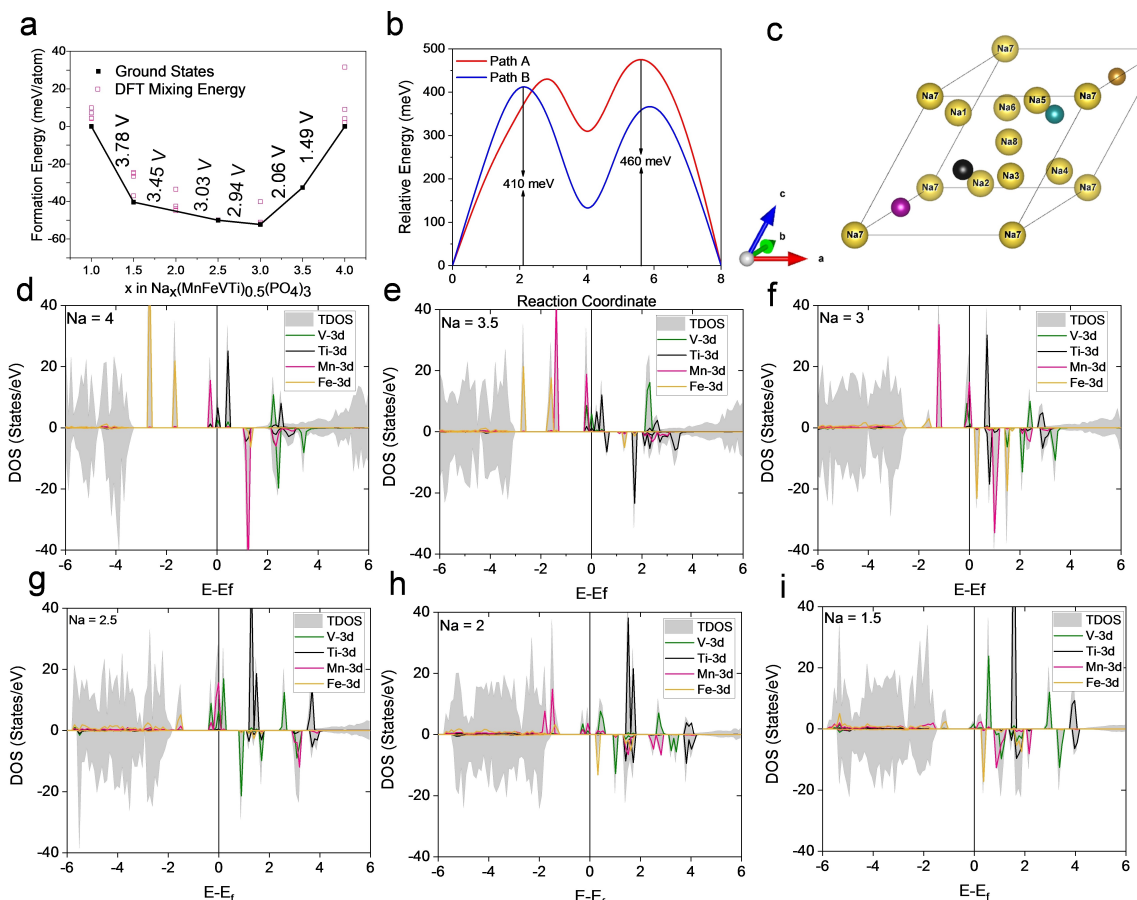


Figure 6. Theoretical studies on NMVTP. a) Formation energies and convex hull of NMVTP. b) Na-migration energy barrier of the NMVTP sample with two different pathways. c) Possible Na^+ -diffusion pathways in NMVTP, and d–i) Density of states calculation focused on the 3d orbitals of the transition metals with respect to the degree of Na^+ extraction from the parent structure.

mined between each pair of compositions, leading to an artificially flat voltage profile that represents the averaged voltage associated with the specific Na concentrations.^[72] More comprehensive voltage curves can potentially be generated using the cluster expansion technique.^[73] Nevertheless, the calculated voltage profile generally closely matches the experimental voltage profile. Ionic diffusivity is a widely recognized factor that significantly influences the performance of electrode materials. It is strongly associated with the electrochemical characteristics of batteries, including their rate capability, cycling performance, and structural stability.^[74] Therefore, we used DFT to model the ion transport process within batteries. To identify the favorable Na-ion pathways in the structure, we scanned various possible pathways by using the SoftBV software.^[75]

The results revealed two unique pathways, i.e., $\text{Na}_8 \rightarrow \text{Na}_1/\text{Na}_2/\text{Na}_3 \rightarrow \text{Na}_7$ and $\text{Na}_8 \rightarrow \text{Na}_4/\text{Na}_5/\text{Na}_6 \rightarrow \text{Na}_7$, referred to as Paths A and B, respectively. Based on our calculations, the barrier energies of Paths A and B are 410 and 460 meV, respectively (Figure 6b). Furthermore, the ranges of migration barriers of LiCoO_2 and the $\text{LiNi}_{0.8}\text{Co}_{0.2}\text{O}_2$ cathode materials are 200–600 and 357–545 meV, respectively.^[76] Previous research estimated that the maximum diffusion barriers of intercalated

cations in micron- and nanosized particles are ≈ 525 and ≈ 650 meV, respectively, for adequate battery operation.^[77] Considering these facts, we can expect that the low energy barrier for Na diffusion in NMVTP materials is a key factor that supports their superior electrochemical performances (Figure 6c). To identify the evolution of oxidation states in transition metals, we calculate the density of states in $\text{Na}_x(\text{MnVFeTi})_0.5(\text{PO}_4)_3$ ($x = 1.5, 2, \dots, 4$) (Figure 6d–i). As shown in Figure 6, all the 3d orbitals in the transition metals are located near the Fermi level. As the desodiation process begins, at $x = 3.5$ and 3, we can observe the split of the Mn-3d and V-3d orbitals, whereas the Ti-3d and Fe-3d shift to the conduction band, indicating $\text{Ti}^{3+/4+}$ and $\text{Fe}^{2+/3+}$ reactions, respectively. As the desodiation process continues, we can observe that the Mn-3d and V-3d orbitals overlap and become the major orbital near the Fermi level. As the process reaches $\text{Na}_2(\text{MnVFeTi})_0.5(\text{PO}_4)_3$, we observe that the Mn-3d and V-3d orbitals shift to the conduction band, indicating $\text{Mn}^{2+/3+}$ and $\text{V}^{4+/5+}$ reactions, respectively. Moreover, the overlapped orbitals shift simultaneously, resulting in small differences of 2.94 and 3.03 V in the desodiation potential. The last stage of desodiation, i.e., $\text{Na}_2(\text{MnVFeTi})_0.5(\text{PO}_4)_3$ changing to $\text{Na}_{1.5}(\text{MnVFeTi})_0.5(\text{PO}_4)_3$, involves $\text{V}^{4+/5+}$ reactions, which is

indicated by the shift of each orbital under the corresponding composition.

It must be acknowledged that a similar composition for SIBs has been reported only in the recent past.^[34] However, this study used a pyro-synthesis technique, known for its single step carbon coating and rapidity (process completed within few minutes). In this study, the combined experimental and theoretical validation of the electrochemical Na⁺ storage performance has been verified, and this constitutes the difference of this study in comparison with the recent report that lacked the theoretical validation. Furthermore, the Na⁺ electrochemical storage mechanism of NMVFTP/C cathodes is analogous to the previous report, confirming the reproducibility of the proposed composition with the different synthesis method, underlining the practical feasibility of NMVFTP/C cathodes.

3. Conclusions

NMVFTP/C, as a new NASICON-type cathode for NIBs, was constructed by the distribution of multi-elements such as V, Mn, Fe and Ti. The multi-electron contribution from V³⁺, Mn²⁺, Fe²⁺, and Ti⁴⁺ increased the Na-storage capacity of the NMVFTP/C cathode and improved the electrochemical stability. *Operando* XRD analysis confirmed that during the charge/discharge process, Na⁺ (de)insertion in the NMVFTP/C cathode followed a reversible single bi-phasic transition. Successively, a reasonable cycle life output of 150 mA g⁻¹ with 91% capacity retention was accomplished after 100 cycles. DFT calculations revealed two unique pathways (Na8→Na1/Na2/Na3→Na7 (Path A) and Na8→Na4/Na5/Na6→Na7 (Path B)) for Na⁺ migration. The excellent electrochemical outputs can be attributed to the low barrier energies for Na⁺ migration following Paths A (410 mV) and B (460 mV).

3.1. Shortcomings and Future Perspectives

The multi-transition metal ion engineering approach is the most effective way to achieve the new composition. There is, however, considerable scope for improvement in ensuring that electrochemically active elements play a full part in sodium storage properties. In particular, the Mn^{2+/3+} electrochemical activity observed in this study is superimposed on the V^{3+/4+} which produces a low initial charge capacity output (99.37 mA h g⁻¹) even with a high Na content of 3.5. It is therefore essential to gain a detailed understanding of the role of the multi-electron transfer properties of the proposed cathode.

Experimental Segment

To prepare the NMVFTP/C sample, the solution combustion-based pyro-synthesis technique is utilized. In detail, the metal precursors including 3.5 mmol of sodium nitrate (Sigma-Aldrich, 99%), 0.5 mmol of manganese nitrate (Sigma-Aldrich, 97%), 0.5 mmol of iron nitrate (Sigma-Aldrich, ≥98%), 0.5 mmol of titanium isobut-

oxide (Sigma-Aldrich, 97%), and 3.0 mmol of phosphoric acid (DAEJUNG, 85%) were dissolved in 200 ml of tetraethylene glycol (Sigma-Aldrich, ≥98%) solvent. The 0.5 mmol of ammonium vanadate (JUNSEI, 99%) precursor is pre-dissolved in 10 ml deionized water in the presence of 1.0 mmol of Oxalic acid (DAEJUNG, 99.5%) and added to the above metal precursors. Once all the metal precursors have been homogeneously dissolved, 50 ml of paint thinner is added as an igniter. This initiates the spontaneous combustion reaction. A rectangular disposable boat made of household aluminum foil is used for the combustion process. The homogeneous solution is filled with 50% of the capacity of the aluminum boat, maintained at 450 °C and subjected to the self-extinguishing combustion reaction. To obtain the carbon-coated NMVFTP/C sample, the combustion deposits were collected and subjected to thermal annealing in an inert Ar atmosphere at 650 °C for 6 h. The carbon-coated NMVFTP/C sample prepared using similar synthetic procedure as documented earlier by our group is used for comparison.

Structural and Physical Characterization

The XRD patterns of the targeted materials in this study is analyzed using the 3D high-resolution X-ray diffractometer (Empyrean, PANalytical, The Netherlands). The morphological features of the cathode were analyzed using field-emission scanning electron microscopy (FE-SEM) using a Hitachi S-4700. Besides, the lattice fringes and selected area electron diffraction patterns (SAED) are observed using the field emission transmission electron microscopy (FE-TEM, 20 kV, Philips Tecnai F20, KBSI Chonnam National University). The carbon content in the NMVFTP/C sample was evaluated using the thermogravimetric analysis (TGA) accomplished using an SDT Q600 thermobalance in air with a temperature gradient of 5 °C min⁻¹. Moreover, the nature of the carbon in the sample is analyzed using the JASCO Raman spectrometer NRS-5100 series. The X-ray photoelectron spectroscopy (XPS, Thermo VG Scientific Multilab 2000) with an Al K α X-ray source is used to analyze the elemental compositions and the oxidation states of the transition metal ions in the NMVFTP/C sample.

Electrochemical Characterization

The working electrodes were made of NMVFTP/C (70 wt%), ketjenblack (15 wt%), and polyacrylic acid (15 wt%) using N-methyl-2pyrrolidone solvent, and the resultant slurry was coated on the carbon-coated aluminium foil. Later, the working electrode is dried in a vacuum oven maintained at 80 °C, and then hot-rolled between the stainless-steel rollers maintained at 120 °C and pressed into round discs with a diameter of 14 mm. The active mass of the working electrode ranged between 2.2–2.9 mg. The coin-cell is fabricated in the argon-filled glovebox using the sodium metal anode in 1 M NaPF₆ in ethylene carbonate: diethylene carbonate (1:1) with 5% fluoroethylene carbonate (FEC) as the electrolyte. The electrochemical properties were tested between 4.2 and 1.5 V using cyclic voltammetry (CV, BioLogic Science Instruments) and galvanostatic charge/discharge measurements using the programmable battery tester (TOYO).

Operando XRD Studies

In house *Operando* XRD measurements using a PANalytical (Empyrean), X-ray diffractometer with Mo K α radiation ($\lambda = 0.070926 \text{ \AA}$) under 60Kv-30Ma, the range of 4.6° to 35°, and step-width of 0.0064° is used to record the electrochemical structural variations of the NMVFTP/C cathode. The *Operando* cell assembled with NMVFTP/C cathode is galvanostatically cycled between 4.2–

1.5 V at a current density of 30 mA g⁻¹ (For the *Operando* cell (Beryllium (Be) acts as a current collector and the X-ray penetration window). The recorded Mo K α radiation patterns were adapted into Cu K α radiation patterns using the linked X'Pert Highscore Plus Program.

5. First-Principle Calculations

We employ the Quantum-Espresso package using GBRV ultra-soft pseudopotential to perform first-principles calculations based on density functional theory (DFT).^[78–80] The “vc-relax” function and Broyden – Fletcher–Goldfarb–Shanno (BFGS) were used to allow the optimization of 2 units cell of NMVFTP which consists of 42 atoms with a plane-wave basis set with a kinetic energy of 544 eV and the convergence criteria are set as 10–6 Ry for electronic loops and 10–3 Ry/Bohr for ionic loops.^[81] For further convex hull calculation, the lowest energy from five different NMVFTP configurations with the lowest electrostatic energies generated by Supercell software developed by Okhotnikov et al was selected.^[82] The Brillouin zones were sampled using 2x2x2 k-point with an energy. To minimize the discrepancies, we therefore utilized Hubbard correction, which is widely implemented for electrode calculations to predict the electrochemical properties despite the slight inaccuracy of the result. To tune the Hubbard value, we follow the previously reported method.^[83] Briefly, we eliminated the error that comes from the over-binding energy of O₂ and followed by finding the U values that give the slightest error of the corresponding oxide compound formation energy compared to the experimental value. Based on this procedure, the maximum error that we obtain is 1.54%. U values are given based on the following table.

To scan the favorable pathways of Na diffusion, the analysis was evaluated using SoftBV software.^[75] To predict the energy barrier more accurately, we use climbing image nudge elastic band method. For each NEB calculation, 9 images were used to ensure that the initial sodium positions in successive images were no more than 0.5 Å from each other. To avoid ambiguity regarding the localization of electrons, no U correction was used. The volume was frozen at the volume of the relaxed

desodiated structure, and only the k-point located at Γ (the Brillouin zone center) was used. To establish the general phase behavior of Na (de)intercalation into the Na_x(MnVFeTi)_{0.5}(PO₄)₃ structure, we construct the convex hull that is consisted of the formation energies of various Na/vacancy orderings at different Na concentrations, x ($1.5 \leq x \leq 4.0$), with respect to the DFT energies of the fully discharged (i.e., E[Na_{3.5}(MnVFeTi)_{0.5}(PO₄)₃]) and fully charged (E[Na(MnVFeTi)_{0.5}(PO₄)₃]) configurations. The relative energy is calculated based on the following equation:

$$E_f(x) = E[Na_x(MnVFeTi)_{0.5}(PO_4)_3] - \frac{4-x}{3}E[Na_1(MnVFeTi)_{0.5}(PO_4)_3] - \frac{x-1}{3}E[Na_4(MnVFeTi)_{0.5}(PO_4)_3]$$

Based on the stable configurations, we calculate the theoretical (de)intercalation potential based on the following equation:

$$V = -\frac{\Delta G^0}{(x-y)F} = \frac{E[(Na_x(MnVFeTi)_{0.5}(PO_4)_3) - E(Na_y(MnVFeTi)_{0.5}(PO_4)_3) + (x-y)\mu_{Na}]}{(x-y)F}$$

5.1. Specific Power and Specific Energy Calculation

Specific Power was calculated as P (W kg⁻¹) = $I \times V / 2 m$

Where I is the applied current (A), V is the average working voltage (V), and m is the mass of the active cathode material.^[84]

Specific Energy was calculated as E (Wh kg⁻¹) = Specific capacity × average working voltage.^[85]

Author Contributions

V. S, G. A, and A. A contributed equally to this manuscript. The manuscript was written through the contributions of all authors.

Table 1. U value calculation from the Hubbard correction.

Compound	Transition Metal Species	U	Calc. Form. Energy (eV)	Exp. Form. Energy (eV)	Error (%)
V ₂ O ₃	V ³⁺	0.5	-2.517	-2.522	0.206
VO ₂	V ⁴⁺	1	-2.467	-2.475	0.314
V ₂ O ₅	V ⁵⁺	1.3	-2.301	-2.296	0.213
Ti ₂ O ₃	Ti ³⁺	0.5	-3.139	-3.153	0.434
TiO ₂	Ti ⁴⁺	0.75	-3.264	-3.261	0.086
MnO	Mn ²⁺	-1.8	-1.965	-1.996	1.540
Mn ₂ O ₃	Mn ³⁺	0	-1.985	-1.983	0.110
MnO ₂	Mn ⁴⁺	1.05	-1.817	-1.797	1.086
FeO	Fe ²⁺	-0.6	-1.408	-1.415	0.472
Fe ₂ O ₃	Fe ³⁺	0	-1.711	-1.71	0.077

Acknowledgements

This study was supported by the National Research Foundation of Korea (NRF) grant funded by the Korean government (MSIT) (NRF-2020R1 A2 C3012415). This research was also supported by the Basic Science Research Program through the National Research Foundation of Korea (NRF), funded by the Ministry of Education (grant number RS-2021-NR060128).

Conflict of Interests

The authors declare no competing financial interests.

Data Availability Statement

The data that support the findings of this study are available from the corresponding author upon reasonable request.

- [1] E. Adhitama, M. M. Bela, F. Demelash, M. C. Stan, M. Winter, A. Gomez-Martin, T. Placke, *Adv. Energy Mater.* **2023**, *13*, 2203256.
- [2] S. Bag, H. Murarka, C. Zhou, A. Bhattacharya, D. Jokhakar, V. G. Pol, V. Thangadurai, *ACS Appl. Energy Mater.* **2020**, *3*, 8475.
- [3] S. Chen, C. Wu, L. Shen, C. Zhu, Y. Huang, K. Xi, J. Maier, Y. Yu, *Adv. Mater.* **2017**, *29*, 1700431.
- [4] V. Soundharajan, D. T. Pham, J. Piao, S. Nithiananth, J. H. Kim, J. Kim, *Batter. Supercaps.* **2024**, *7*, e202400131.
- [5] H. R. Sarma, J. Sun, I. E. Gunathilaka, Y. Hora, M. Forsyth, N. Byrne, *Sustain. Mater. Technol.* **2024**, *39*, e00846.
- [6] T. Bashir, S. Zhou, S. Yang, S. A. Ismail, T. Ali, H. Wang, J. Zhao, L. Gao, *Electrochem. Energy Rev.* **2023**, *6*, 5.
- [7] X. Song, X. Li, H. Shan, J. Wang, W. Li, K. Xu, K. Zhang, H. M. K. Sari, L. Lei, W. Xiao, J. Qin, C. Xie, X. Sun, *Adv. Funct. Mater.* **2024**, *34*, 2303211.
- [8] Y. Xi, X. Wang, H. Wang, M. Wang, G. Wang, J. Peng, N. Hou, X. Huang, Y. Cao, Z. Yang, D. Liu, X. Pu, G. Cao, R. Duan, W. Li, J. Wang, K. Zhang, K. Xu, J. Zhang, X. Li, *Adv. Funct. Mater.* **2024**, *34*, 2309701.
- [9] Z. Tang, S. Zhou, Y. Huang, H. Wang, R. Zhang, Q. Wang, D. Sun, Y. Tang, H. Wang, *Electrochem. Energy Rev.* **2023**, *6*, 8.
- [10] Y. Chen, Q. Li, P. Wang, X. Liao, J. Chen, X. Zhang, Q. Zheng, D. Lin, K. Lam, *Small.* **2023**, *19*, 2304002.
- [11] V. Soundharajan, S. Nithiananth, K. Sakthiabirami, J. J. H. Kim, C.-Y. Su, J.-K. Chang, J. Lee, K. Sakthiabirami, D. T. Pham, J. J. H. Kim, J.-Y. Hwang, J. J. H. Kim, *J. Mater. Chem. A.* **2022**, *10*, 1022.
- [12] H. Thu Duong, N. Thi Duong, H. Ngoc bui, S. Nithiananth, V. Soundharajan, D. T. Pham, *J. Electroanal. Chem.* **2024**, *961*, 118227.
- [13] J. Wang, J. Zhao, X. He, Y. Qiao, L. Li, S.-L. Chou, *Sustain. Mater. Technol.* **2022**, *33*, e00446.
- [14] R. Yang, L. Mei, Y. Fan, Q. Zhang, H.-G. Liao, J. Yang, J. Li, Z. Zeng, *Nat. Protoc.* **2023**, *18*, 555.
- [15] Z. Zeng, P. Barai, S.-Y. Lee, J. Yang, X. Zhang, W. Zheng, Y.-S. Liu, K. C. Bustillo, P. Ercius, J. Guo, Y. Cui, V. Srinivasan, H. Zheng, *Nano Energy* **2020**, *72*, 104721.
- [16] S. Ohno, W. G. Zeier, *Nat. Energy* **2022**, *7*, 686.
- [17] H. Pan, Y.-S. Hu, L. Chen, *Energy Environ. Sci.* **2013**, *6*, 2338.
- [18] V. Soundharajan, S. Nithiananth, G. Alfaza, J. Piao, D. T. Pham, E. H. Ang, J. Kasnatscheew, M. Winter, J. H. Kim, J. Kim, *J. Mater. Chem. A.* **2024**, *12*, 11403.
- [19] K. Chayambuka, G. Mulder, D. L. Danilov, P. H. L. Notten, *Adv. Energy Mater.* **2018**, *8*, 1800079.
- [20] X. Zhang, X. Rui, D. Chen, H. Tan, D. Yang, S. Huang, Y. Yu, *Nanoscale* **2019**, *11*, 2556.
- [21] X. Liang, J.-Y. Hwang, Y.-K. Sun, *Adv. Energy Mater.* **2023**, *13*, 2301975.
- [22] Y. Huang, X. Li, J. Wang, L. Miao, C. Li, J. Han, Y. Huang, *Energy Storage Mater.* **2018**, *15*, 108.
- [23] Y. Liu, X. Rong, R. Bai, R. Xiao, C. Xu, C. Zhang, J. Xu, W. Yin, Q. Zhang, X. Liang, Y. Lu, J. Zhao, L. Chen, Y.-S. Hu, *Nat. Energy* **2023**, *8*, 1088.
- [24] H. Gao, I. D. Seymour, S. Xin, L. Xue, G. Henkelman, J. B. Goodenough, *J. Am. Chem. Soc.* **2018**, *140*, 18192.
- [25] X. Liang, X. Ou, F. Zheng, Q. Pan, X. Xiong, R. Hu, C. Yang, M. Liu, *ACS Appl. Mater. Interfaces.* **2017**, *9*, 13151.
- [26] V. Soundharajan, M. H. Alfaruqi, S. Lee, B. Sambandam, S. Kim, S. Kim, V. Mathew, D. T. Pham, J.-Y. Hwang, Y.-K. Sun, J. Kim, *J. Mater. Chem. A.* **2020**, *8*, 12055.
- [27] V. Soundharajan, M. H. Alfaruqi, G. Alfaza, J. Lee, S. Lee, S. Park, S. Nithiananth, D. T. Pham, J.-Y. Hwang, J. Kim, *J. Mater. Chem. A.* **2023**, *11*, 15518.
- [28] M. Ihsan-Ul-Haq, J. Cui, N. Mubarak, M. Xu, X. Shen, Z. Luo, B. Huang, J.-K. Kim, *Adv. Energy Sustain. Res.* **2021**, *2*, 2100072.
- [29] V. Soundharajan, S. Lee, S. Park, J. Piao, V. Mathew, J. Kim, *Chem. Eng. J.* **2023**, *472*, 144994.
- [30] Y. Jiang, Z. Yang, W. Li, L. Zeng, F. Pan, M. Wang, X. Wei, G. Hu, L. Gu, Y. Yu, *Adv. Energy Mater.* **2015**, *5*, 1402104.
- [31] X. Shen, Y. Su, S. He, Y. Li, L. Xu, N. Yang, Y. Liao, M. Wang, F. Wu, J. Mater. Chem. A. **2023**, *11*, 16860.
- [32] Z. Wu, F. Ye, Q. Liu, R. Pang, Y. Liu, L. Jiang, Z. Tang, L. Hu, *Adv. Energy Mater.* **2022**, *12*, 2200654.
- [33] A. K. Padhi, K. S. Nanjundaswamy, C. Masquelier, J. B. Goodenough, *J. Electrochem. Soc.* **1997**, *144*, 2581.
- [34] M. Li, C. Sun, X. Yuan, Y. Li, Y. Yuan, H. Jin, J. Lu, Y. Zhao, *Adv. Funct. Mater.* **2024**, *34*, 2314019.
- [35] V. Soundharajan, S. Kim, S. Nithiananth, M. H. Alfaruqi, J. Piao, D. T. Pham, V. Mathew, S. A. Han, J. H. Kim, J. Kim, *Carbon Energy* **2024**, *6*, e551. [https://doi.org/10.1002/cey2.551..](https://doi.org/10.1002/cey2.551)
- [36] W. Zhou, L. Xue, X. Lü, H. Gao, Y. Li, S. Xin, G. Fu, Z. Cui, Y. Zhu, J. B. Goodenough, *Nano Lett.* **2016**, *16*, 7836.
- [37] S. L. Dreyer, R. Zhang, J. Wang, A. Kondrakov, Q. Wang, T. Brezesinski, J. Janek, *J. Phys. Energy* **2023**, *5*, 035002.
- [38] C. Zhao, F. Ding, Y. Lu, L. Chen, Y.-S. Hu, *Angew. Chem. Int. Ed.* **2020**, *59*, 264.
- [39] L. Zhu, M. Wang, S. Xiang, D. Sun, Y. Tang, H. Wang, *Adv. Energy Mater.* **2023**, *13*, 2302046.
- [40] M. Li, C. Sun, Q. Ni, Z. Sun, Y. Liu, Y. Li, L. Li, H. Jin, Y. Zhao, *Adv. Energy Mater.* **2023**, *13*, 2203971.
- [41] N. Doebelin, R. Kleeberg, *J. Appl. Crystallogr.* **2015**, *48*, 1573.
- [42] K. Momma, F. Izumi, *J. Appl. Crystallogr.* **2011**, *44*, 1272.
- [43] M. Klinger, A. Jager, *J. Appl. Crystallogr.* **2015**, *48*, 2012.
- [44] J. Li, X. Zhao, P. He, Y. Liu, J. Jin, Q. Shen, Y. Wang, S. Li, X. Qu, Y. Liu, L. Jiao, *Small.* **2022**, *18*, 2202879.
- [45] B. Sambandam, V. Soundharajan, J. Song, S. Kim, J. Jo, P. T. Duong, S. Kim, V. Mathew, J. Kim, *J. Power Sources* **2017**, *350*, 80.
- [46] T. Wu, J. Sun, Z. Q. Jeremy Yap, M. Ke, C. Y. H. Lim, L. Lu, *Mater. Des.* **2020**, *186*, 108287.
- [47] S. Nithiananth, S. Harish, J. Archana, M. Navaneethan, M. Shimomura, *Mater. Lett.* **2020**, *264*, 127354.
- [48] X. Cao, Q. Sun, L. Zhu, L. Xie, *J. Alloys Compd.* **2019**, *791*, 296.
- [49] B. Sambandam, V. Soundharajan, J. Song, S. Kim, J. Jo, D. P. Tung, S. Kim, V. Mathew, J. Kim, *Inorg. Chem. Front.* **2016**, *3*, 1609.
- [50] L. Bi, X. Li, X. Liu, Q. Zheng, D. Lin, *ACS Sustain. Chem. Eng.* **2019**, *7*, 7693.
- [51] S. Sun, Y. Chen, Q. Bai, Z. Tian, Q. Huang, C. Liu, S. He, Y. Yang, Y. Wang, L. Guo, *Chem. Eng. J.* **2023**, *451*, 138780.
- [52] H. T. Nguyen, D. Jung, C.-Y. Park, D. J. Kang, *Mater. Chem. Phys.* **2015**, *165*, 19.
- [53] L. Gao, H. Zhan, C. Zhang, M. Cao, *Diam. Relat. Mater.* **2024**, *148*, 111453.
- [54] J. C. Shao, Q. Y. Meng, X. R. Dou, H. Z. Chi, *Electrochim. Acta.* **2024**, *473*, 143468.
- [55] J. Li, Q. Yuan, J. Hao, R. Wang, T. Wang, L. Pan, J. Li, C. Wang, *Inorg. Chem.* **2023**, *62*, 17745.
- [56] F. L. Lama, V. Marangon, Á. Caballero, J. Morales, J. Hassoun, *ChemSusChem* **2023**, *16*, e202202095.
- [57] T. Zhou, J. Li, Y. Wang, L. Guo, Y. Chen, *Appl. Surf. Sci.* **2023**, *639*, 158213.
- [58] C. Sun, Q. Ni, M. Li, Z. Sun, X. Yuan, L. Li, K. Wang, H. Jin, Y. Zhao, *Adv. Funct. Mater.* **2024**, *34*, 2310248.
- [59] Q. Zhu, J. Wu, R. Tong, W. Li, X. Hu, N. Tian, L. He, Y. Li, Z. Wang, *J. Alloys Compd.* **2023**, *960*, 170748.
- [60] D. Wang, X. Bie, Q. Fu, D. Dixon, N. Bramnik, Y.-S. Hu, F. Fauth, Y. Wei, H. Ehrenberg, G. Chen, F. Du, *Nat. Commun.* **2017**, *8*, 15888.

- [61] B. Wu, G. Hou, E. Kovalska, V. Mazanek, P. Marvan, L. Liao, L. Dekanovsky, D. Sedmidubsky, I. Marek, C. Hervoches, Z. Sofer, *Inorg. Chem.* **2022**, *61*, 4092.
- [62] Z.-Y. Gu, J.-Z. Guo, J.-M. Cao, X.-T. Wang, X.-X. Zhao, X.-Y. Zheng, W.-H. Li, Z.-H. Sun, H.-J. Liang, X.-L. Wu, *Adv. Mater.* **2022**, *34*, 2110108.
- [63] J. Chen, Y. Huang, J. Liu, C. Li, H. Zheng, X. Xu, L. Fu, X. Li, M. Wang, Y. Lin, H. Cao, *Electrochim. Acta* **2023**, *458*, 142521.
- [64] H. Li, M. Xu, C. Gao, W. Zhang, Z. Zhang, Y. Lai, L. Jiao, *Energy Storage Mater.* **2020**, *26*, 325.
- [65] H. Li, Y. Wang, X. Zhao, J. Jin, Q. Shen, J. Li, Y. Liu, X. Qu, L. Jiao, Y. Liu, *ACS Energy Lett.* **2023**, *8*, 3666.
- [66] P. Hu, T. Zhu, C. Cai, X. Wang, L. Zhang, L. Mai, L. Zhou, *Angew. Chem. Int. Ed.* **2023**, *62*, e202219304.
- [67] J. Hou, M. Hadouchi, L. Sui, J. Liu, M. Tang, Z. Hu, H.-J. Lin, C.-Y. Kuo, C.-T. Chen, C.-W. Pao, Y. Huang, J. Ma, *Small* **2023**, *19*, 2302726.
- [68] S. Park, J.-N. Chotard, D. Carlier, F. Fauth, A. Iadecola, C. Masquelier, L. Croguennec, *Chem. Mater.* **2023**, *35*, 3181.
- [69] W. Zhang, Y. Wu, Y. Dai, Z. Xu, L. He, Z. Li, S. Li, R. Chen, X. Gao, W. Zong, F. Guo, J. Zhu, H. Dong, J. Li, C. Ye, S. Li, F. Wu, Z. Zhang, G. He, Y. Lai, I. P. Parkin, *Chem. Sci.* **2023**, *14*, 8662.
- [70] T. Chen, J. Yang, L. Barroso-Luque, G. Ceder, *ACS Energy Lett.* **2023**, *8*, 314.
- [71] J. Vergnet, M. Saubanère, M.-L. Doublet, J.-M. Tarascon, *Joule* **2020**, *4*, 420.
- [72] M. K. Aydinol, A. F. Kohan, G. Ceder, *J. Power Sources* **1997**, *68*, 664.
- [73] A. Van der Ven, M. K. Aydinol, G. Ceder, *J. Electrochem. Soc.* **1998**, *145*, 2149.
- [74] Q. He, B. Yu, Z. Li, Y. Zhao, *Energy Environ. Mater.* **2019**, *2*, 264.
- [75] L. L. Wong, K. C. Phuah, R. Dai, H. Chen, W. S. Chew, S. Adams, *Chem. Mater.* **2021**, *33*, 625.
- [76] Z. Jadidi, T. Chen, P. Xiao, A. Urban, G. Ceder, *J. Mater. Chem. A* **2020**, *8*, 19965.
- [77] Z. Rong, R. Malik, P. Canepa, G. Sai Gautam, M. Liu, A. Jain, K. Persson, G. Ceder, *Chem. Mater.* **2015**, *27*, 6016.
- [78] W. Kohn, L. J. Sham, *Phys. Rev.* **1965**, *140*, A1133.
- [79] P. Giannozzi, S. Baroni, N. Bonini, M. Calandra, R. Car, C. Cavazzoni, D. Ceresoli, G. Chiarotti, M. Cococcioni, I. Dabo, A. Corso, S. de Gironcoli, S. Fabris, G. Fratesi, R. Gebauer, U. Gerstmann, C. Gougoussis, A. Kokalj, M. Lazzeri, R. Wentzcovitch, *J. Phys. Condens. Matter.* **2009**, *21*, 395502.
- [80] K. F. Garrity, J. W. Bennett, K. M. Rabe, D. Vanderbilt, *Comput. Mater. Sci.* **2014**, *81*, 446.
- [81] C. G. Broyden, *IMA J. Appl. Math.* **1970**, *6*, 76.
- [82] K. Okhotnikov, T. Charpentier, S. Cadars, *J. Cheminform.* **2016**, *8*, 17.
- [83] L. Wang, T. Maxisch, G. Ceder, *Phys. Rev. B* **2006**, *73*, 195107.
- [84] V. Soundharajan, B. Sambandam, S. Kim, V. Mathew, J. Jo, S. Kim, J. Lee, S. Islam, K. Kim, Y.-K. Sun, J. Kim, *ACS Energy Lett.* **2018**, *3*, 1998.
- [85] V. Soundharajan, B. Sambandam, S. Kim, M. H. Alfaruqi, D. Y. Putro, J. Jo, S. Kim, V. Mathew, Y.-K. Sun, J. Kim, *Nano Lett.* **2018**, *18*, 2402.

Manuscript received: July 31, 2024

Revised manuscript received: September 18, 2024

Accepted manuscript online: September 22, 2024

Version of record online: November 16, 2024